Resilient High Precision Positioning using RTK and Distributed GNSS Antenna Subarrays

Can Özmaden[1], Marius Brachvogel[1], Tobias Bamberg[1,2], Michael Niestroj[1], Michael Meurer[1,2]
[1] *Chair of Navigation, RWTH Aachen University, Germany*
[2] *Institute of Communications and Navigation, German Aerospace Center (DLR), Germany*

BIOGRAPHY

Can Özmaden is a Ph.D. student and a research associate at the Chair of Navigation of RWTH Aachen University in Germany. He received his M.Sc. degree in Electrical Engineering, Information Technology and Computer Engineering from RWTH Aachen University in 2023. His research interests include navigation and positioning for autonomous applications, and novel positioning techniques.

Marius Brachvogel received his Master of Science in electrical engineering from RWTH Aachen University in 2016. Following his activity as a student assistant, he joined the Chair of Navigation as a scientific researcher after graduation to pursue his Ph.D. His research is located in the field of GNSS signal processing with focus on spatial processing techniques for interference and spoofer mitigation in distributed array systems for autonomous driving.

Tobias Bamberg received his M.Sc. in electrical engineering from RWTH Aachen University in 2017. He completed his Master thesis in the field of GNSS spoofing detection and mitigation. In November 2017 he joined the Institute of Communications and Navigation of the German Aerospace Center (DLR) in Oberpfaffenhofen and began his doctorate studies at RWTH Aachen University. His main research interest lies on the development of resilient and precise multi-antenna GNSS receivers focused on the signal processing layer.

Michael Niestroj received his Master of Science in electrical engineering from RWTH Aachen University in 2016. His master thesis covered attitude and calibration estimation for multi antenna GNSS receivers. He is currently pursuing his Ph.D. at RWTH Aachen University as a member of the Chair of Navigation. His research is focused on calibration methods for GNSS multi antenna systems and techniques for the localization of sources of interference.

Michael Meurer received the diploma in electrical engineering and the Ph.D. degree from the University of Kaiserslautern, Germany. After graduation, he joined the Research Group for Radio Communications at the Technical University of Kaiserslautern, Germany, as a senior key researcher, where he was involved in various international and national projects in the field of communications and navigation both as project coordinator and as technical contributor. From 2003 till 2013, Dr. Meurer was active as a senior lecturer and Associate Professor (PD) at the same university. Since 2006 Dr. Meurer is with the German Aerospace Center (DLR), Institute of Communications and Navigation, where he is the director of the Department of Navigation and of the center of excellence for satellite navigation. In addition, since 2013 he is a professor of electrical engineering and director of the Chair of Navigation at the RWTH Aachen University. His current research interests include GNSS signals, GNSS receivers, interference and spoofing mitigation and navigation for safety-critical applications.

ABSTRACT

The emergence of applications such as autonomous vehicles and UAVs (Unmanned Aerial Vehicles) has lately brought high precision positioning into the focus of the GNSS (Global Navigation Satellite System) community. Simultaneously, such autonomous applications fall under the category of SoL (Safety of Life), applications and therefore require strict protection levels, high integrity, and resilience against GNSS interference. Protection and toughening of GNSS receivers against jamming and spoofing has been a heavily studied subject in the last decade. Literature has proven spatial signal processing algorithms combined with compact antenna arrays to show effectiveness in providing the required resilience. However, due to the large footprint of these arrays, the distribution of smaller subarrays has been considered more aesthetic by the industry and customers alike. Such distributed systems can be installed more discretely and in various synthetic parts of a vehicle. This paper studies such a distributed antenna subarray system in a series of real-world measurements under the use of carrier-phase based RTK (Real Time Kinematics) positioning. The goal of the paper is to meet the requirements of high precision and resilient positioning. A demonstration of sustained high precision positioning under jamming conditions is presented using spatial signal processing algorithms. A statistical analysis is carried out to compare single antenna processing approach against a multi-antenna spatial signal processing one. Assessment of a state-of-the-art carrier-phase compensation algorithm for spatial interference mitigation filter is made to study its benefits for RTK-based positioning using multi-antenna setups.

https://doi.org/10.33012/2023.19276

I. INTRODUCTION

Modern land, maritime and air traffic are unimaginable without the accurate, highly available, and continuous GNSS-based PNT (Positioning, Navigation, and Timing). In the near future, the influence and wide-spread use of GNSS is only expected to rise further as projected by annual report of the European Union Agency for Space Programme (EUSPA, 2022). Self-driving cars, in their various levels of autonomy, and drones in the form of air taxis or delivery UAVs are becoming a growing reality. These emergent technologies use a plethora of sensors for local and relative situational awareness, such as IMUs (Inertial Measurement Units), radar, LiDAR, and cameras. Nevertheless, GNSS remains the sole provider of absolute global positioning and therefore crucial in the context of sensor fusion as identified by Reid et al. (2019).

Unfortunately, one of the biggest shortcomings of GNSS-based positioning is its innate susceptibility to RF (Radio Frequency) interference. In their seminal article, Pullen and Gao (2012) show that GNSS jammers do not require a high level of technical complexity to overwhelm commercially available GNSS receivers. Gao et al. (2013) also show that, albeit non-malicious in their intent, sources of interference, such as other aviation radio navigation systems, impede the positioning capabilities of a GNSS receiver all the same. Once the receiver is jammed, positioning capabilities are lost. A significant recovery time is required for the resumption of nominal operation, even if the interference time window was brief. The severity of jamming in the context of civil aviation are experimentally demonstrated by Osechas et al. (2022).

In recent decades, literature and practice have shown the effectiveness of antenna arrays combined with spatial signal processing techniques in mitigating GNSS interference (Cuntz et al., 2007; Gao et al., 2016; Morales-Ferre et al., 2020; Taşdemir et al., 2018). Such multi-antenna systems can be steered electronically to amplify the wanted satellite signals, and simultaneously suppress unwanted RF interference sources. Moreover, the effects of multipath signals can also be mitigated by using multi-antenna GNSS systems.

However, one major drawback of antenna arrays are their relatively large footprint, hindering aesthetic installation considerations. Brachvogel et al. (2020) state that the autonomous vehicle industry regards this factor as playing a pivotal role in the highly-competitive consumer mass market. For instance, a typical URA (Uniform Rectangular Array) configuration for the GNSS L1 frequency band, occupies around 20 to $25\,\mathrm{cm}^2$. This footprint results from physical constrains, requiring adjacent antenna elements to be spaced half a wavelength apart. A promising solution to this problem is provided in the aforementioned work (Brachvogel et al., 2020) by splitting large antenna arrays into smaller, spatially distributed ULA (Uniform Linear Array) subarrays. Consequently, these can be installed in a more discrete manner, in different locations on the vehicle.

Applying carrier-phase based positioning methods on compact GNSS antenna arrays has been a topic of recent research in the GNSS community (Bamberg et al., 2023; Daneshmand et al., 2016; Kappen et al., 2022). This paper explores the use of carrier-phase based positioning under the use of distributed GNSS antenna subarrays.

Related Work

a) RTK and Multi-Antenna GNSS

Medina et al. (2020) have explored carrier-phase based positioning using multi-antenna GNSS systems. A joint positioning and attitude estimation problem is solved by linearizing the measurement model and applying an Extended Kalman Filter. However, the authors are concerned solely with attitude and pose estimation, and do not process the multi-antenna GNSS system with spatial signal processing techniques. Thus, resilience against interference is left unexplored. The utilized multi-antenna setup also does not constitute a compact antenna array setup, but can be rather classified as a multi-receiver setup.

Yoder and Humphreys (2023) have investigated the use of multi-antenna GNSS in conjunction with carrier phase based positioning, vehicle dynamic constrains, and IMU integration in a dynamic urban environment scenario. The authors used the multi-antenna GNSS system to solely estimate the attitude of the vehicle and combine estimates with those from other sensors. This approach does not employ multi-antenna spatial signal processing techniques. In a previous related work, Clements et al. (2022) have demonstrated single antenna spoofing mitigation capabilities using the same sensor platform. However, this still leaves an investigation into the effects of jamming under the use of multi-antenna spatial signal processing and RTK-based positioning unanswered.

Bamberg and Meurer (2020) identified and quantified the carrier-phase distortions induced by spatial signal processing algorithms like MVDR. In their subsequent work they present a phase compensation algorithm to rectify the carrier-phase observable after spatial filtering (Bamberg et al., 2023). Authors also experimentally validate the algorithms by reaching a sub-meter precision under jamming conditions. However, a large footprint URA system is used, leaving RTK-based positioning with spatially distributed subarrays an unexplored topic.

b) Spatially Distributed Antenna Subarrays

Brachvogel et al. (2020) propose a novel antenna configuration, by splitting the elements of a common URA into two spatially distributed ULA subarrays. These two configurations can be seen contrasted in Figure 1 The work is further developed in Brachvogel et al. (2023) by calibrating the mismatches occurring due to the cable lengths. The authors, however, did not evaluate the positioning solutions using carrier-phase based algorithms.

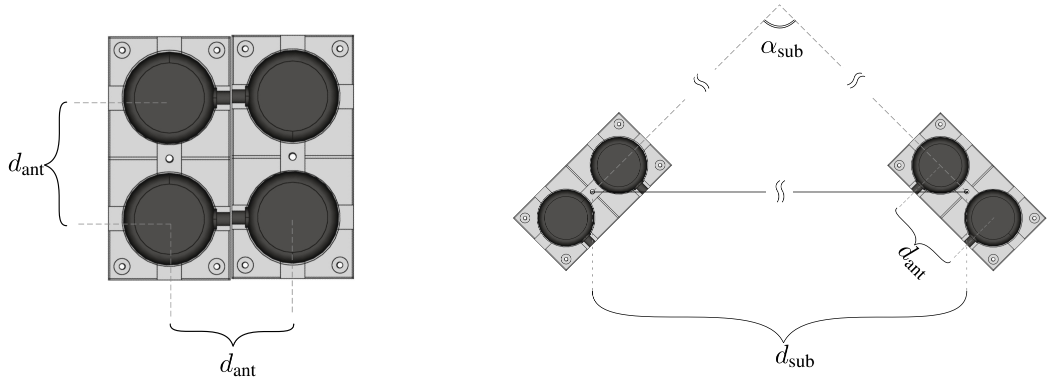

(a) 2×2 Uniform Rectangular Array (URA)   **(b)** Distributed Antenna Subarrays

Figure 1: Comparison of the two antenna array configurations.

Contributions

The aim of this paper is to investigate novel approaches in designing systems utilizing both RTK-based positioning and spatially distributed GNSS antenna subarrays. The contributions are as follows:

- Demonstration of distributed antenna subarrays achieving an RTK fix using real world measurements.
- Demonstration of jamming resilience of distributed antenna subarrays, while maintaining an RTK fix.
- Marginal performance degradation in comparison to classical URA configured multi-antenna systems.

II. SIGNAL MODEL

1. Multi-Antenna Signal Model

a) Received Signal for a Single Antenna Receiver

A GNSS signal received from the k-th satellite by a single antenna can be modeled as:

$$\underline{s}^{(k)}(t) = A s_{\mathrm{b}}^{(k)}(t) \mathrm{e}^{\mathrm{j}2\pi\left(f_{\mathrm{c}}+f_{\mathrm{D}}^{(k)}\right)t+\varphi^{(k)}} + \underline{n}(t), \tag{1}$$

where the baseband signal $s_{\mathrm{b}}^{(k)}$ expands to:

$$s_{\mathrm{b}}^{(k)}(t) = d^{(k)}(t-\tau^{(k)})c^{(k)}(t-\tau^{(k)}) \tag{2}$$

and

A is an arbitrary amplitude of an RF signal, proportional to the transmission power $P_{\mathrm{t}}^{(k)}$ of the k-th satellite.

$d^{(k)}$ is data signal containing the navigation message payload,

$c^{(k)}$ is a unique CDMA (Code Division Multiple Access) PRN (Pseudo Random Noise) code of the k-th satellite, by which $d^{(k)}$ is spread,

$\tau^{(k)}$ is the time delay of the PRN code corresponding to the signal travel time,

f_{c} denotes the carrier frequency of the signal,

$f_{\mathrm{D}}^{(k)}$ the experienced Doppler shift due to relative movement,

$\varphi^{(k)}$ the carrier phase shift, and

$\underline{n}(t)$ is a complex zero mean AWGN (Additive White Gaussian Noise) term with a standard deviation of σ_n:

$$\underline{n}(t) \sim \mathcal{N}(0, \sigma_n^2)$$

b) *Received Signal for a Multi-Antenna Receiver*

We depart from the single antenna model of the Equation (2) by considering an arbitrary amount of antennas $N_{\text{ant}} > 1, N_{\text{ant}} \in \mathbb{Z}$ forming an array. Let the antennas be arbitrarily distributed in space, with a certain body frame position vector $\boldsymbol{r}_i^{\text{b}}$ describing the position of an i-th antenna, $i \in \{1 \dots N_{\text{ant}}\}$. Due to spatial separation between the antenna elements, a signal arriving from the k-th satellite will experience an additional time delay denoted by $\delta\tau_i^{(k)}$ depending on the location of the i-th antenna. Thus, the total delay of the signal for the i-th antenna $\tau_{\text{tot},i}^{(k)}$ will consist of:

$$\tau_{\text{tot},i}^{(k)} = \tau^{(k)} + \delta\tau_i^{(k)},$$

where $\tau^{(k)}$ is the code delay defined for the origin of the body frame coordinate system.

A GNSS signal transmitted by the k-th satellite and received by N_{ant} antennas can be then expressed as:

$$\underline{\boldsymbol{s}}^{(k)}(t) = \underline{\boldsymbol{\gamma}}(t) \odot \begin{bmatrix} \underline{s}(t - \delta\tau_1^{(k)}) \\ \underline{s}(t - \delta\tau_2^{(k)}) \\ \vdots \\ \underline{s}(t - \delta\tau_{N_{\text{ant}}}^{(k)}) \end{bmatrix}, \tag{3}$$

with each row of the vector equivalent to a time delayed received signal from Equation (1), and where $\odot$ denotes the Hadamard product. The term $\underline{\boldsymbol{\gamma}}$ is of great importance, and is a DOA-dependent (Direction Of Arrival) complex gain factor modelling the amplitude and phase mismatches between the N_{ant} antennas in the front end of the receiver. This term is frequently referred to as a *calibration vector* in the literature, and has to be estimated separately to achieve coherent results when processing multi-antenna systems. In our following discussion this term is assumed to be perfectly known, and calibrated for via state-of-the-art estimation techniques (Zorn et al., 2017). Additionally, it should be noted that Equation (3) neglects the cross-talk effects between the antennas, that would have yielded a calibration matrix $\underline{\boldsymbol{\Gamma}} \in \mathbb{C}^{N_{\text{ant}} \times N_{\text{ant}}}$. However, those are found to be negligible for GNSS signals by Zorn et al. (2017) and irrelevant for the further discussion of this paper.

Following the conventions set by Van Trees (2002), the relationship between the location of the antenna $\boldsymbol{r}_i^{\text{b}}$, location of the satellite in the sky $\boldsymbol{r}^{\text{b}(k)}$ and the resulting additional time delay $\delta\tau_i^{(k)}$ is given by:

$$\delta\tau_i^{(k)}(t) = -\frac{1}{c_0}\left[\boldsymbol{u}_i^{\text{b}(k)}(t)\right]^{\text{T}} \boldsymbol{r}_i^{\text{b}}, \tag{4}$$

where c_0 denotes the speed of light, and $\boldsymbol{u}_i^{\text{b}(k)}(t)$ denotes the time dependent LOS-vector (Line Of Sight) in the body frame between the k-th satellite and i-th antenna given by:

$$\boldsymbol{u}_i^{\text{b}(k)}(t) = \begin{bmatrix} \cos\left(\phi_i^{(k)}(t)\right)\cos\left(\vartheta_i^{(k)}(t)\right) \\ \sin\left(\phi_i^{(k)}(t)\right)\cos\left(\vartheta_i^{(k)}(t)\right) \\ \sin\left(\vartheta_i^{(k)}(t)\right), \end{bmatrix} \tag{5}$$

with ϕ and ϑ denoting the azimuth and elevation angles to the satellite respectively. It can be derived via coordinate transformation following Groves (2008) between the body frame position $\boldsymbol{r}_i^{\text{b}}$ and navigation frame position $\boldsymbol{r}_k^{\text{n}}$. In general the distances between antenna elements can be assumed to be far smaller than the range between the antennas and the satellite:

$$\begin{gathered} \left\|\boldsymbol{r}_\mu^{\text{e}} - \boldsymbol{r}_\nu^{\text{e}}\right\|_2 \ll \left\|\boldsymbol{r}^{\text{e}(k)} - \boldsymbol{r}_i^{\text{e}}\right\|_2, \\ \forall i \in \{1 \dots N_{\text{ant}}\} \wedge \forall k \in \{1 \dots K\} \wedge \mu, \nu \in \{1 \dots N_{\text{ant}}\} \wedge \mu \neq \nu. \end{gathered} \tag{6}$$

With this assumption, the LOS-vector is defined once for the origin of the body frame and held constant across all antennas, simplifying Equations (4) and (5) to be antenna independent.

For narrowband signals, such as GPS (Global Positioning System) L1, the time delay between the antenna elements $\delta\tau_i$ can be expressed as a phase shift of the carrier wave. Thus, the baseband signal s_{b} can be assumed not affected by the time delay $\delta\tau_i$.

From Equation (3), this yields:

$$\underline{\boldsymbol{s}}^{(k)}(t) = \underline{s}_{\mathrm{b}}^{(k)}(t)\mathrm{e}^{\mathrm{j}2\pi\left(f_{\mathrm{c}}+f_{\mathrm{D}}^{(k)}\right)t}\underbrace{\begin{bmatrix}\mathrm{e}^{-\mathrm{j}2\pi\left(f_{\mathrm{c}}+f_{\mathrm{D}}^{(k)}\right)\delta\tau_1^{(k)}(t)}\\ \mathrm{e}^{-\mathrm{j}2\pi\left(f_{\mathrm{c}}+f_{\mathrm{D}}^{(k)}\right)\delta\tau_2^{(k)}(t)}\\ \vdots\\ \mathrm{e}^{-\mathrm{j}2\pi\left(f_{\mathrm{c}}+f_{\mathrm{D}}^{(k)}\right)\delta\tau_{N_{\mathrm{ant}}}^{(k)}(t)}\end{bmatrix}}_{\underline{\boldsymbol{a}}^{(k)}(t)} + \underline{\boldsymbol{n}}(t), \tag{7}$$

where $\underline{\boldsymbol{a}}^{(k)}(t)$ is referred to as the *steering vector* in array processing literature (Van Trees, 2002). This assumption, however, does not hold true for growing distances between the antenna elements d_{ant} and for modern wideband GNSS signals such as GPS L5 or Galileo E5a. Effects of this have been studied by Brachvogel et al. (2021) and calibrated for in a related further work by Brachvogel et al. (2023) using STAP (Space Time Adaptive Processing).

2. Interference and Spatial Signal Processing

This section introduces the spatial signal processing techniques for the signal defined in Equation (7).

a) No interference case

Considering all K satellites, and no interfering signals, the sum signal can be modeled as:

$$\underline{\boldsymbol{x}}(t) = \sum_{k=1}^{K}\underline{\boldsymbol{s}}^{(k)} + \underline{\boldsymbol{n}}(t) \tag{8}$$

Neglecting the quantization effects, by sampling the signal with the sampling rate f_{s} we get the following time-discrete representation of the previously continuous signal:

$$\underline{\boldsymbol{x}}[\ell] = \underline{\boldsymbol{x}}\left(\frac{t}{\ell T_{\mathrm{s}}}\right),$$

where $T_{\mathrm{s}} = \frac{1}{f_{\mathrm{s}}}$ is the sampling duration, and the square brackets $[\cdot]$ indicate time-discrete samples, such that a block of L samples becomes:

$$\underline{\boldsymbol{X}}[\ell] = \underline{\boldsymbol{S}}[\ell] + \underline{\boldsymbol{N}}[\ell], \tag{9}$$

where $\underline{\boldsymbol{X}}[\ell], \underline{\boldsymbol{S}}[\ell], \underline{\boldsymbol{N}}[\ell] \in \mathbb{C}^{N_{\mathrm{ant}}\times L}$. The matrix notation of the sampled GNSS signal $\underline{\boldsymbol{S}}[\ell]$ in Equation (9) expanded as follows:

$$\underline{\boldsymbol{S}}[\ell] = \begin{bmatrix}\underline{s}_1[(\ell-1)L+1] & \underline{s}_1[(\ell-1)L+2] & \dots & \underline{s}_1[(\ell-1)L+L]\\ \underline{s}_2[(\ell-1)L+1] & \underline{s}_2[(\ell-1)L+2] & \dots & \underline{s}_2[(\ell-1)L+L]\\ \vdots & \vdots & \ddots & \vdots\\ \underline{s}_{N_{\mathrm{ant}}}[(\ell-1)L+1] & \underline{s}_{N_{\mathrm{ant}}}[(\ell-1)L+2] & \dots & \underline{s}_{N_{\mathrm{ant}}}[(\ell-1)L+L]\end{bmatrix} \tag{10}$$

b) Interference case

In the case of arbitrary M interfering signals, each interference source reads:

$$\underline{\boldsymbol{z}}^{(m)}(t) = \begin{bmatrix}\underline{z}_{\mathrm{b}}^{(m)}(t-\delta\tau_1^{(m)})\mathrm{e}^{\mathrm{j}2\pi\left(f_{\mathrm{t}}+f_{\mathrm{D}}^{(m)}\right)t}\\ \underline{z}_{\mathrm{b}}^{(m)}(t-\delta\tau_2^{(m)})\mathrm{e}^{\mathrm{j}2\pi\left(f_{\mathrm{t}}+f_{\mathrm{D}}^{(m)}\right)t}\\ \vdots\\ \underline{z}_{\mathrm{b}}^{(m)}(t-\delta\tau_{N_{\mathrm{ant}}}^{(m)})\mathrm{e}^{\mathrm{j}2\pi\left(f_{\mathrm{t}}+f_{\mathrm{D}}^{(m)}\right)t}\end{bmatrix} \odot \underbrace{\begin{bmatrix}\mathrm{e}^{-\mathrm{j}2\pi\left(f_{\mathrm{t}}+f_{\mathrm{D}}^{(m)}\right)\delta\tau_1^{(m)}(t)}\\ \mathrm{e}^{-\mathrm{j}2\pi\left(f_{\mathrm{t}}+f_{\mathrm{D}}^{(m)}\right)\delta\tau_2^{(m)}(t)}\\ \vdots\\ \mathrm{e}^{-\mathrm{j}2\pi\left(f_{\mathrm{t}}+f_{\mathrm{D}}^{(m)}\right)\delta\tau_{N_{\mathrm{ant}}}^{(m)}(t)}\end{bmatrix}}_{\underline{\boldsymbol{a}}^{(m)}(t)}, \tag{11}$$

where $\underline{z}_{\mathrm{b}}^{(m)}$ is an arbitrarily defined baseband signal of the m-th interference source that is modulated onto a carrier with the frequency of f_{t}, and experiencing a Doppler shift of $f_{\mathrm{D}}^{(m)}$. Just as previously in Equation (11), $\underline{\boldsymbol{a}}^{(m)}$ denotes the array steering vector, though this time it contains the DOA characteristics of the m-th interference source.

Rewriting Equation (9) in the presence of such interference signals yields:

$$\underline{\boldsymbol{X}}[\ell] = \underline{\boldsymbol{S}}[\ell] + \underline{\boldsymbol{J}}[\ell] + \underline{\boldsymbol{N}}[\ell], \tag{12}$$

c) Pre-whitening

In this paper a blind spatial signal processing technique introduced and described by Sgammini et al. (2012) is utilized to suppress GNSS interference. The GNSS receiver modified to take up this task is illustrated in Figure 2.

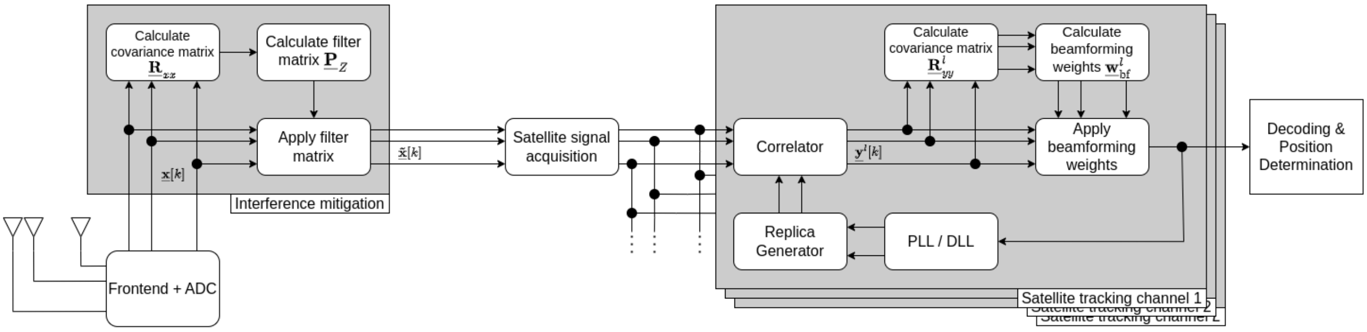

Figure 2: Block Diagram of a Multi-Antenna GNSS Receiver consisting of the two-step interference mitigation and beamforming approach.

First step in the utilized blind spatial signal processing technique is the *pre-correlation* filtering. Due to the low power of the GNSS signals, we can assume the covariance of the antenna signal from Equation (12) to be spatially and temporally white (Sgammini et al., 2012), i.e. for $M = 0$:

$$\mathcal{H}_0 : \underline{\boldsymbol{X}}(t) \sim \mathcal{N}(0, \underline{\boldsymbol{R}}_{\text{nn}}), \tag{13}$$

where $\mathcal{H}_0$ denotes the *null hypothesis*, case without interference.

Following Sgammini et al. (2012), we can express the spatial covariance of $\underline{\boldsymbol{X}}$ in the presence of interference as:

$$\underline{\boldsymbol{R}}_{\text{xx}}[\ell] = \underline{\boldsymbol{X}}[\ell]\underline{\boldsymbol{X}}^{\text{H}}[\ell] \approx \underline{\boldsymbol{R}}_{\text{ss}}[\ell] + \underline{\boldsymbol{R}}_{\text{zz}}[\ell] + \underline{\boldsymbol{R}}_{\text{nn}}[\ell] \tag{14}$$

This is due to the fact that GNSS signals and interference sources can be assumed to be uncorrelated. The same is argued for the additive white Gaussian spatial noise. In the next step, due to the low power of GNSS signals, the term $\underline{\boldsymbol{R}}_{\text{ss}}[\ell]$ can be neglected, yielding:

$$\begin{aligned} \underline{\boldsymbol{R}}_{\text{xx}}[\ell] &\approx \underline{\boldsymbol{R}}_{\text{zz}}[\ell] + \underline{\boldsymbol{R}}_{\text{nn}}[\ell] \\ &= \underline{\boldsymbol{R}}_{\text{zz}}[\ell] + \sigma_n^2 \boldsymbol{I} \end{aligned} \tag{15}$$

Thus, we can detect the presence of interference from testing following hypothesis:

$$\mathcal{H}_1 : \underline{\boldsymbol{X}}(t) \sim \mathcal{N}(0, \underline{\boldsymbol{R}}_{\text{zz}} + \underline{\boldsymbol{R}}_{\text{nn}}), \tag{16}$$

where $\mathcal{H}_1$ denotes the *interference hypothesis*. We can apply an eigendecomposition scheme on the covariance $\underline{\boldsymbol{R}}_{\text{zz}}$, leading to:

$$\underline{\boldsymbol{R}}_{\text{zz}} = \underline{\boldsymbol{U}}_{\text{z}} \underline{\boldsymbol{\Lambda}}_{\text{z}} \underline{\boldsymbol{U}}_{\text{z}}^{\text{H}} = \underline{\boldsymbol{U}}_{\text{z}} \begin{bmatrix} \lambda_{z,1} & 0 & \cdots & 0 \\ 0 & \lambda_{z,2} & \cdots & 0 \\ \vdots & \vdots & \ddots & \vdots \\ 0 & 0 & \cdots & \lambda_{z,M} \end{bmatrix} \underline{\boldsymbol{U}}_{\text{z}}^{\text{H}}, \tag{17}$$

where $\underline{\boldsymbol{\Lambda}}_{\text{z}}$ represents the diagonal matrix containing non-zero eigenvalues of the interference subspace. We can devise a filter by considering:

$$\underline{\boldsymbol{R}}_{\text{xx}}^{-\frac{1}{2}}[\ell] \approx \underbrace{\underline{\boldsymbol{U}}_{\text{z}} \left(\underline{\boldsymbol{\Lambda}}_{\text{z}} + \sigma_n^2 \boldsymbol{I}_{\text{z}} \right)^{-\frac{1}{2}} \underline{\boldsymbol{U}}_{\text{z}}^{\text{H}}}_{\to 0 \quad \text{for strong interference, i.e. } \lambda_i >> \sigma_n^2} + \underbrace{\frac{1}{\sqrt{\sigma_n^2}} \underline{\boldsymbol{U}}_n \underline{\boldsymbol{U}}_n^{\text{H}}}_{\equiv \underline{\boldsymbol{P}}}, \tag{18}$$

Thus, the so-called *pre-whitening filter* $\underline{\boldsymbol{P}}$ filters each input sample $\underline{\boldsymbol{x}}[\ell]$ as follows:

$$\underline{\tilde{\boldsymbol{x}}}[\ell] = \underline{\boldsymbol{P}}[\ell]\underline{\boldsymbol{x}}[\ell], \tag{19}$$

where $\underline{\boldsymbol{P}}$ can be alternatively expanded as per Brachvogel et al. (2020):

$$\underline{\boldsymbol{P}}[\ell] = \frac{\sqrt{N_{\text{ant}}}}{\left\|\underline{\boldsymbol{R}}_{xx}^{-\frac{1}{2}}[\ell]\right\|_{\text{F}}}\underline{\boldsymbol{R}}_{xx}^{-\frac{1}{2}}[\ell] \tag{20}$$

Pre-whitening the input signal $\underline{\boldsymbol{X}}$ yields the new covariance:

$$\underline{\boldsymbol{R}}_{\tilde{\text{x}}\tilde{\text{x}}}[\ell] \approx \underbrace{\underline{\boldsymbol{P}}[\ell]\underline{\boldsymbol{R}}_{\text{ss}}[\ell]\underline{\boldsymbol{P}}[\ell]}_{\text{filtered GNSS signals}} + \underbrace{0}_{\text{interference term}} + \underbrace{\underline{\boldsymbol{R}}_{\tilde{n}\tilde{n}}[\ell]}_{\text{filtered noise}} \tag{21}$$

d) Beamforming

The beamformer also operates blindly, that is by considering the correlation between the antenna channels without a-priori information about satellite sources. Due to performing an eigendecomposition, in literature this beamformer is often called an eigenbeamformer. The beamformer operates on the baseband signal $\underline{\boldsymbol{y}}$ after code wipe-off, which is where the signal is elevated from the noise floor. Per Sgammini et al. (2012), the covariance of $\underline{\boldsymbol{y}}$ can be written as:

$$\underline{\boldsymbol{R}}_{yy} = \lambda_{\text{d}}\underline{\boldsymbol{u}}_{\text{d}}\underline{\boldsymbol{u}}_{\text{d}}^{\text{H}} + \underline{\boldsymbol{U}\boldsymbol{\Lambda}\boldsymbol{U}}^{\text{H}} + \frac{\sigma_n^2}{L}\boldsymbol{I}_{N_{\text{ant}}}, \tag{22}$$

where λ_{d} is the dominant non-zero eigenvalue from the signal covariance matrix $\underline{\boldsymbol{R}}_{ss}$. A beamformer operating on the output of a correlator can be generally written as:

$$\underline{y}[\ell] = \boldsymbol{w}^{\text{H}}\underline{\boldsymbol{y}}[\ell], \tag{23}$$

where $\underline{\boldsymbol{w}}$ represents the complex weights of the beamformer. The eigenbeamformer is the beamformer that optimizes the following problem, and it is defined simply as:

$$\underline{\boldsymbol{w}} = \underline{\boldsymbol{u}}_{\text{d}} \tag{24}$$

since this solves the optimization problem of:

$$\max_{\underline{\boldsymbol{w}}} \frac{\underline{\boldsymbol{w}}^{\text{H}}\lambda_d\underline{\boldsymbol{u}}_d\underline{\boldsymbol{u}}_d^{\text{H}}\underline{\boldsymbol{w}}}{\underline{\boldsymbol{w}}^{\text{H}}\left(\underline{\boldsymbol{U}\boldsymbol{\Lambda}\boldsymbol{U}}^{\text{H}} + \frac{\sigma_n^2}{L}\mathbf{I}_{N_{\text{ant}}}\right)\underline{\boldsymbol{w}}}. \tag{25}$$

III. METHODOLOGY

The following section summarizes the data acquisition and processing techniques behind the results presented in the later sections.

1. Experiment Setup

To experiment and test the RTK-based positioning with spatially distributed antenna subarrays a series of real world measurements were planned and conducted. To minimize systematic errors due to physical movements and vibration, a 3D-printed experiment setup was designed illustrated in Figure 3. The 3D-printed parts are kept modular and adaptable to various configurations. Main degrees of freedom of the modular 3D-desined antenna mounts are related to the physical dimensions:

- Distance between antennas for one subarray element d_{ant},
- Distance between the subarray elements d_{sub},
- Angle subtended by the subarray elements α_{sub}.

2. Data Acquisition and Analysis

Three different experiments were conducted that are summarized in Table 1. The naming of the antenna elements and how the rig was positioned is illustrated in Figure 4. It can be seen that the subarray setup was placed on top of a metallic structure. This way no other metallic structure was found nearby blocking view towards the sky. In Figures 5a and 5b the measurement setup of Measurement C is illustrated. This was the sole measurement conducted in a GNSS-denied environment. The jamming antenna can be seen on the left-hand side in Figure 5a. It is a directional log-periodic antenna placed 5 m away from the subarray setup,

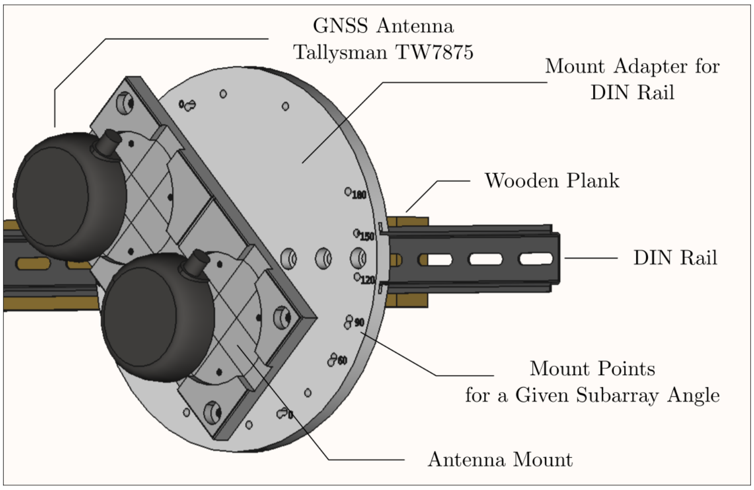

Figure 3: CAD view of the antenna mount used for the experiments in this paper.

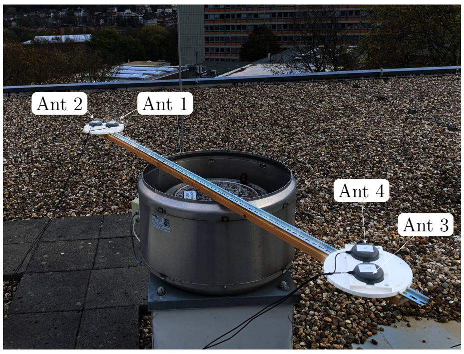

Figure 4: Measurement setup on the UMIC Building rooftop of the RWTH Aachen University, Germany.

and pointing directly at it. A band limited Gaussian noise signal was selected to be the jamming signal, possessing a bandwidth of 5 MHz, and thus covering main lobes of GPS L1 C/A (Coarse / Aquisiton). This way the worst jammer scenario is simulated, in contrast to e.g. a continuous wave jammer that could have been simply filtered out by a notch filter in the frontend of the receiver, without the need for spatial signal processing.

	Measurements		
	A	B	C
Date & Time in UTC	2023-01-18 10:26:19	2023-01-18 10:41:01	2023-01-18 10:58:31
Duration in minutes	10	10	10
Configuration	URA	Subarray	Subarray
Jamming	-	-	static+dynamic

Table 1: Measurement setup description

The acquired raw IQ-data from the SDR (Software Defined Radio) platform is first post-processed by an in-house GNSS SDR receiver. The processed observations are written into a RINEX (Receiver independent exchange format) observation file, and combined with an observation RINEX file from the local SAPOS (Satellitenpositionierungsdienst der deutschen Landesvermessung) reference station, and a merged navigation RINEX ephemeris file fed to the RTKPOS application of the RTKLIB.

(a) Jammer antenna **(b)** GNSS antenna subarrays

Figure 5: Measurement setup of a GNSS-denied environment.

Conducted measurements possess a certain duration, during which more than one position is calculated on an epoch-by-epoch basis. RTKLIB writes these solutions into a so-called *positioning solution file* with an extension of `.pos` (Takasu, 2013). Each line inside this `.pos` file correspond to a filtered RTK-based positioning solution.

The measurements are conducted under static conditions, though slight deviations due to noise make subsequent positions not equal to each other. Naturally, the question arises which one of these solutions is the desired one. Our estimand is the true position of the i-th antenna $\boldsymbol{r}_i^{\mathrm{e}}$. By this, the geometric center of the antenna is meant, which is further biased due to the antenna phase-offset term $\Delta\boldsymbol{r}_{\mathrm{PO}}^{\mathrm{e}}$.

We can extract a series of ECEF (Earth-Centered Earth-Fixed) positions of the i-th antenna from the i-th antennas' `.pos` file as:

$$\hat{\boldsymbol{r}}_i^{\mathrm{e}} = \begin{bmatrix} \hat{\boldsymbol{r}}_i^{\mathrm{e}}[1] & \hat{\boldsymbol{r}}_i^{\mathrm{e}}[2] & \dots & \hat{\boldsymbol{r}}_i^{\mathrm{e}}[N_{\mathrm{pos}}] \end{bmatrix} \tag{26}$$

$$= \left[\begin{pmatrix} \hat{x}_i^{\mathrm{e}}[1] \\ \hat{y}_i^{\mathrm{e}}[1] \\ \hat{z}_i^{\mathrm{e}}[1] \end{pmatrix} \quad \begin{pmatrix} \hat{x}_i^{\mathrm{e}}[2] \\ \hat{y}_i^{\mathrm{e}}[2] \\ \hat{z}_i^{\mathrm{e}}[2] \end{pmatrix} \quad \dots \quad \begin{pmatrix} \hat{x}_i^{\mathrm{e}}[N_{\mathrm{pos}}] \\ \hat{y}_i^{\mathrm{e}}[N_{\mathrm{pos}}] \\ \hat{z}_i^{\mathrm{e}}[N_{\mathrm{pos}}] \end{pmatrix} \quad \right], \tag{27}$$

where $\boldsymbol{r}[\kappa]$ denotes the κ-th position such that $\{\kappa \in \mathbb{Z} | 1 \leq \kappa \leq N_{\mathrm{pos}}\}$. RTK position solutions are categorized into float and fix solutions. Per defintion, float and fix positioning solutions form a disjoint set:

$$\boldsymbol{r}_{\mathrm{fx}}^{\mathrm{e}} \cap \boldsymbol{r}_{\mathrm{ft}}^{\mathrm{e}} = \emptyset, \tag{28}$$

and assuming no outages they are both proper subsets of the entire series of ECEF positions such that:

$$\boldsymbol{r}^{\mathrm{e}} = \boldsymbol{r}_{\mathrm{fx}}^{\mathrm{e}} \cup \boldsymbol{r}_{\mathrm{ft}}^{\mathrm{e}}. \tag{29}$$

The desired true position of the i-th antenna $\boldsymbol{r}_i^{\mathrm{e}}$ is assumed to be embedded in the series of estimated positions $\hat{\boldsymbol{r}}_i^{\mathrm{e}}$ as follows:

$$\hat{\boldsymbol{r}}_i^{\mathrm{e}}[\kappa] = \boldsymbol{r}_i^{\mathrm{e}} + \Delta\boldsymbol{r}_{i,\mathrm{PO}}^{\mathrm{e}} + \boldsymbol{n}[\kappa], \tag{30}$$

where $\boldsymbol{n}[\kappa] \in \mathbb{R}^{1\times 3}$ is random noise variable, causing a deviation from the true position $\boldsymbol{r}_i^{\mathrm{e}}$. This relationship is best visualized in Figure 6, where a point cloud of estimated antenna positions is depicted outside the housing of the antenna to illustrate the

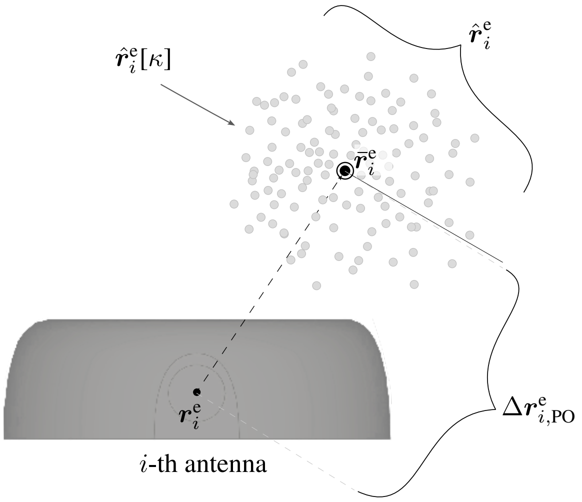

Figure 6: Illustration of the estimated position deviation in 2D.

extreme case of $\Delta\boldsymbol{r}_{i,\mathrm{PO}}^{\mathrm{e}}$. For float solutions $\boldsymbol{r}_{i,\mathrm{ft}}^{\mathrm{e}}$ the noise term will dominate over the hardware term, i.e.

$$\boldsymbol{n}[\kappa] \gg \Delta\boldsymbol{r}_{i,\mathrm{PO}}^{\mathrm{e}} \forall \hat{\boldsymbol{r}}_i^{\mathrm{e}}[\kappa] = \boldsymbol{r}_{i,\mathrm{ft}}^{\mathrm{e}} \tag{31}$$

For fix solutions, we can postulate that the deviation from the true position dramatically decreases, such that:

$$\boldsymbol{n}[\kappa] \ll \Delta\boldsymbol{r}_{i,\mathrm{PO}}^{\mathrm{e}} \forall \hat{\boldsymbol{r}}_i^{\mathrm{e}}[\kappa] = \boldsymbol{r}_{i,\mathrm{fx}}^{\mathrm{e}} \tag{32}$$

Assuming a long enough observation, with diverse satellite geometry, the noise term approaches AWGN, thus:

$$\boldsymbol{r}_{i,\mathrm{fx}}^{\mathrm{e}} \sim \mathcal{N}(\boldsymbol{r}_i^{\mathrm{e}} + \Delta\boldsymbol{r}_{i,\mathrm{PO}}^{\mathrm{e}}, \boldsymbol{\Sigma}), \tag{33}$$

where $\boldsymbol{\Sigma} \in \mathbb{R}^{3\times 3}$ denotes the covariance matrix of the AWGN process. We can define a simple sample mean estimator as follows (Kay, 1993):

$$\bar{\boldsymbol{r}}_i^{\mathrm{e}} = \frac{1}{N_{\mathrm{pos}}} \sum_{\kappa=1}^{N_{\mathrm{pos}}} \boldsymbol{r}_{i,\mathrm{fx}}^{\mathrm{e}}[\kappa], \tag{34}$$

This estimator will be biased:

$$\mathbb{E}\left[\bar{\boldsymbol{r}}_i^{\mathrm{e}}\right] - \boldsymbol{r}_i^{\mathrm{e}} = \Delta\boldsymbol{r}_{i,\mathrm{PO}}^{\mathrm{e}} \tag{35}$$

IV. RESULTS

1. URA Configuration

a) Measurement A: URA Single Antenna Processing

First the observations gathered from the URA configured measurement are presented. This is the most obvious and least innovative setup, except for the fact that the URA elements have been constructed via subarrays. Due to the fact that URA based algorithms have been consistently tested in the literature, the URA configuration serves as a robust baseline for the subsequent sections.

Illustration of the positioning solutions in a three-dimensional view is given in Figure 7. Figure 7 demonstrates that the cluster of positioning solutions lie all on the rooftop of the UMIC building. Additionally, Figure 7 demonstrates that the URA configuration outlines, namely the rectangular footprint, can be discerned when observing the fix solutions. For the purposes of this visualization the altitude of the positioning solutions has been selected to be geodetically referenced. This is configured in the `.kml` output settings of RTKLIB.

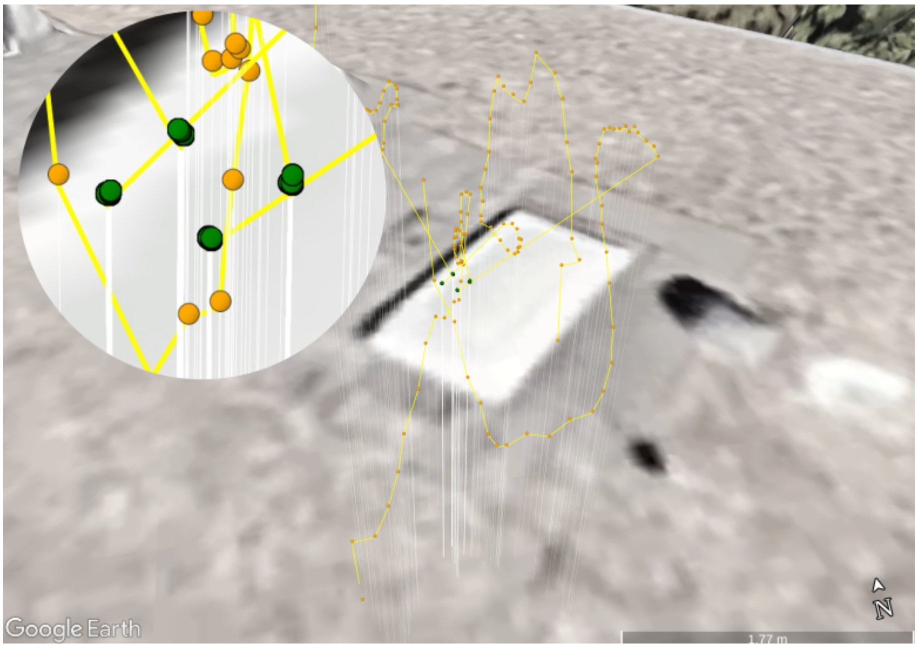

Figure 7: Measurement A: Google Earth imagery of the URA configuration. Zoomed in. Fix solutions are marked green, float solutions orange.

We can evaluate the received signal strength of the satellites under this configuration by examining the C/N_0 metric. As can be seen in Figure 8a, the signal strength levels of the satellites used for the positioning solution lie between 35 dBHz to 50 dBHz.

The PRN G15 is chosen here since it's the RTK pivot satellite to better illustrate the relationship between the diagrams on the left and right-hand side of Figure 8a. For example, we observe a temporal variation of the signal strength of 3 dBHz to 6 dBHz when processing Antenna 1. The right-hand diagram suggests a median value of C/N_0 of approximately 45 dBHz. A greater variance of C/N_0 of G15 is revealed when examining the same diagram on the right, about 8 dBHz to 9 dBHz. This result suggests a high variation of the perceived signal strength across antennas, possibly attributed to uncalibrated hardware differences.

The positioning solution resulting from single antenna processing of the URA configuration is presented in Figure 8b. This is done in three local navigation frame directions: East, North, and Up. The origin of the local frame is selected to be the center of mass of positions, defined by a mean position in Equation (34). Observing and comparing the solutions on the left and right-hand side, one can notice a three order of magnitude of precision improvement once an RTK fix is achieved. Specifically, the deviations from the estimated center position of the antenna lie between -2 mm to 2 mm for fix positions.

b) Measurement A: URA Multi-Antenna Spatial Processing

As introduced in Section III., the outputs of the individual antennas can also be processed jointly by employing spatial signal processing. In this configuration a reference antenna is needed, to which the phase offsets corresponding time delays between the antenna elements are referenced. For instance, by choosing Antenna 1 as the reference antenna, a new virtual antenna is created. The positioning solution produced by a beamformed system is also anchored to this referenced antenna. We can vary the reference antenna among the four antenna elements in URA to get positioning solutions referenced closer to any sought real reference antenna location.

Observing the C/N_0 metric for the spatial signal processing of URA measurements in Figure 9a we can observe the following:

- The median C/N_0 has increased from around 45 dBHz in Figure 9a to 51 dBHz, marking an expected array gain of 6 dB.
- Observing the picked PRN G15, C/N_0 deviations can be tested for statistical significance. Comparing the whiskers of the boxplot in Figure 8a to those in Figure 9a, it is observed that the total spread of C/N_0 values has stayed roughly the same at around 8 dBHz to 9 dBHz.
- Continuing this observation of G15, we can further notice that the IQR (Interquartile range) has also stayed the same at around 2 dBHz to 3 dBHz.

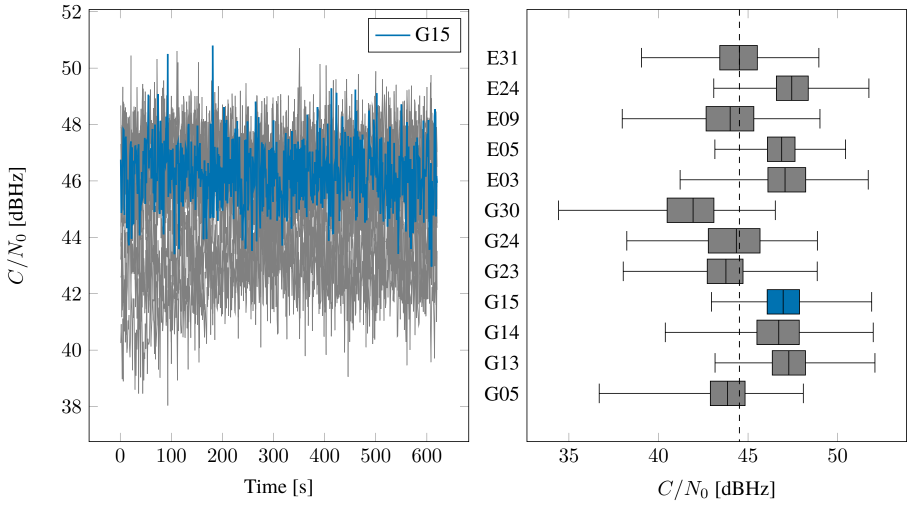

(a) Carrier-to-noise density ratios of the single antenna processing under URA configuration. On the left, the carrier-to-noise density ratios are plotted over time from reference Antenna 1. On the right, all ratios from $N_{\text{ant}} = 4$ are collected. The dashed line represents the median C/N_0.

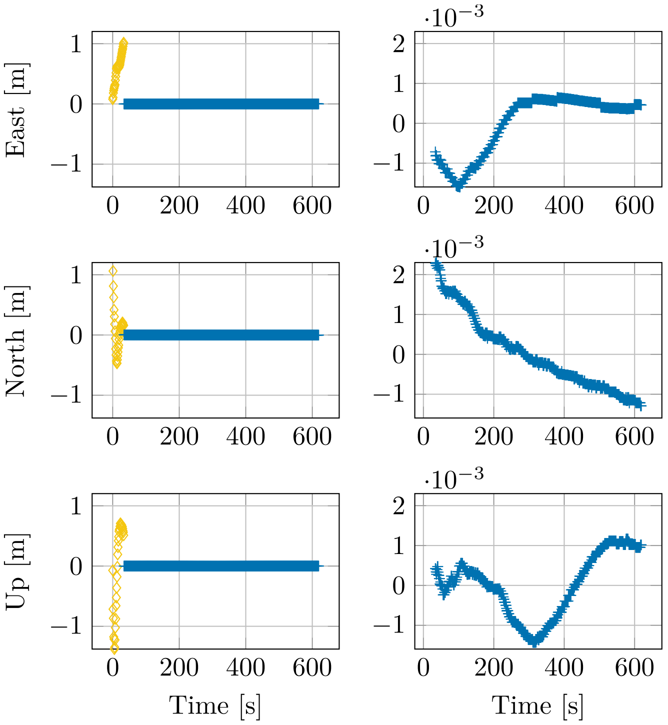

(b) Positioning solution in the local navigation frame (ENU) for Antenna 2. Origin is the center of mass of all fix positions. Yellow points represent float solutions, blue points indicate fix solutions. Plots on the right-hand side are zoomed-in views of fix solutions from the respective axes on the left-hand side.

Figure 8: Measurement A: URA configuration Single Antenna Processing

2. GNSS Denied Environment

a) Measurement C: Distributed Subarrays Single Antenna Processing

Single antenna processing does not provide resilience in a GNSS-denied environment, As presented in previous section, we can analyze the signal strengths of the tracked satellites by observing the C/N_0 metric. The carrier-to-noise density ratios are visualized in Figure 10a. By observing the left-hand side of Figure 10a, we notice an abrupt drop in the measured C/N_0 values of all satellites. This drastic drop occurs at the time instant of the activation of the jammer antenna at around 11:04:29 UTC. The duration for which the jammer was active is tinted orange over time on the plot. The effect of this drop can be observed on the right-hand side of Figure 10a. It illustrates the distribution of C/N_0 values over all antennas of subarray configuration. We notice

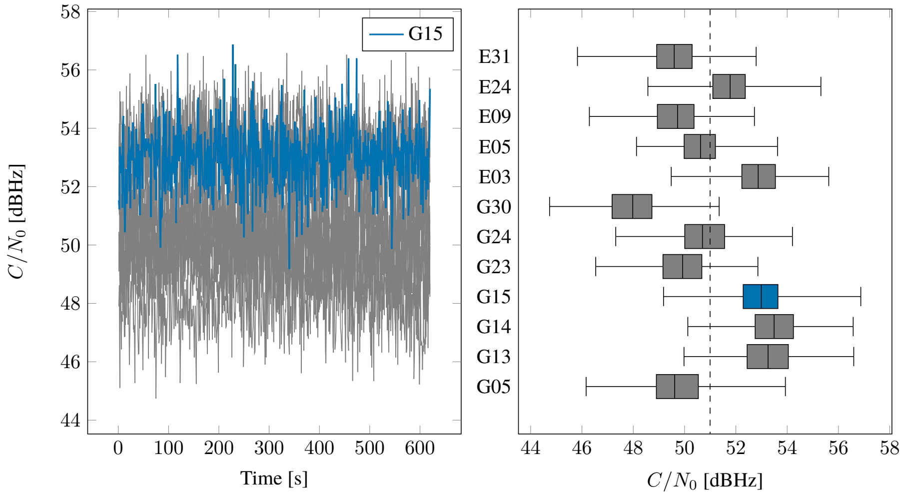

(a) Carrier-to-noise density ratios of the multi-antenna processing under URA configuration. On the left, the carrier-to-noise density ratios are plotted over time from reference Antenna 1. On the right, all ratios from $N_{\text{ant}} = 4$ are collected. The dashed line represents the median C/N_0.

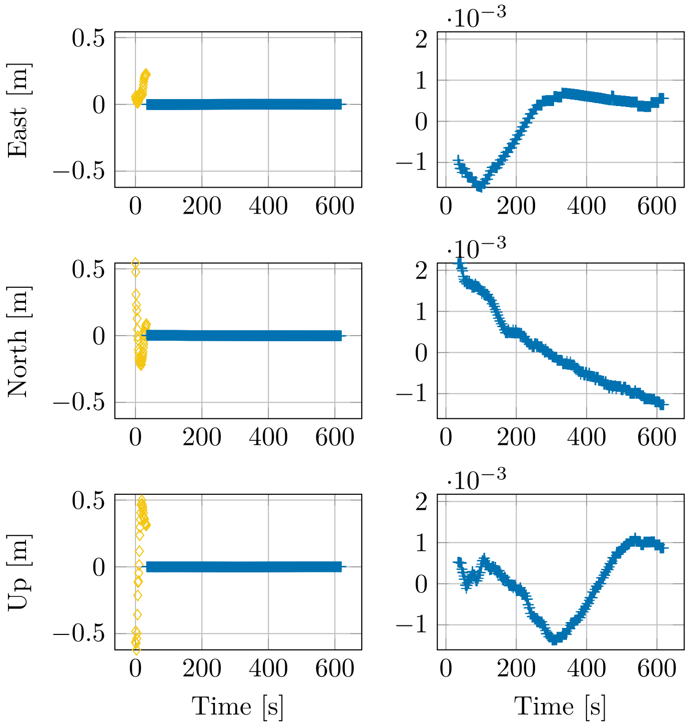

(b) Positioning solution in the local navigation frame (ENU) for Antenna 2. Origin is the center of mass of all fix positions. Yellow points represent float solutions, blue points indicate fix solutions. Plots on the right-hand side are zoomed-in views of fix solutions from the respective axes on the left-hand side.

Figure 9: Measurement A: URA configuration Multi-Antenna Processing

the median value of C/N_0, indicated by the dashed line, remains the same, around 46 dBHz, as in other single antenna processing runs in Figure 8a. However, in contrast to the mentioned figure, Figure 10a illustrates a drastically wider range of C/N_0 values. Notice the skewness of the graph towards 0 dBHz, this directly correlates to the abrupt drop in C/N_0 of all satellites after jamming activates. We can illustrate positioning in the ENU (East North Up) coordinate system, as presented in Figure 10b. Here we notice that during active jamming, indicated by the orange tint on the plot, no fix or positioning solution whatsoever is achieved. Before this time point, an RTK fixed is achieved of identical precision to those presented in previous sections of this chapter. Only the Up direction is observed to pass the ±2 mm line.

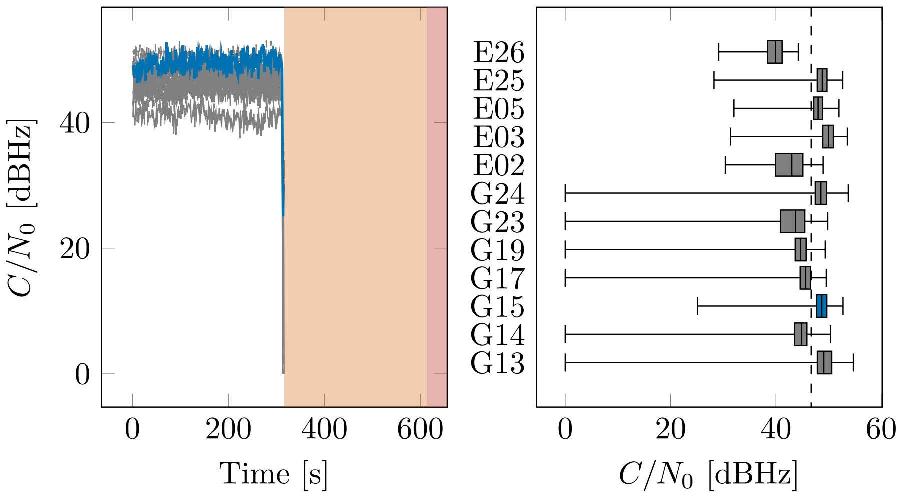

(a) Carrier-to-noise density ratios of the single antenna processing under subarray configuration and in a GNSS-denied environment. On the left, the carrier-to-noise density ratios are plotted over time from reference Antenna 1. The orange background time interval indicates active jamming. On the right, all carrier-to-noise density ratios from $N_{\text{ant}} = 4$ are collected. The dashed line represents the median C/N_0.

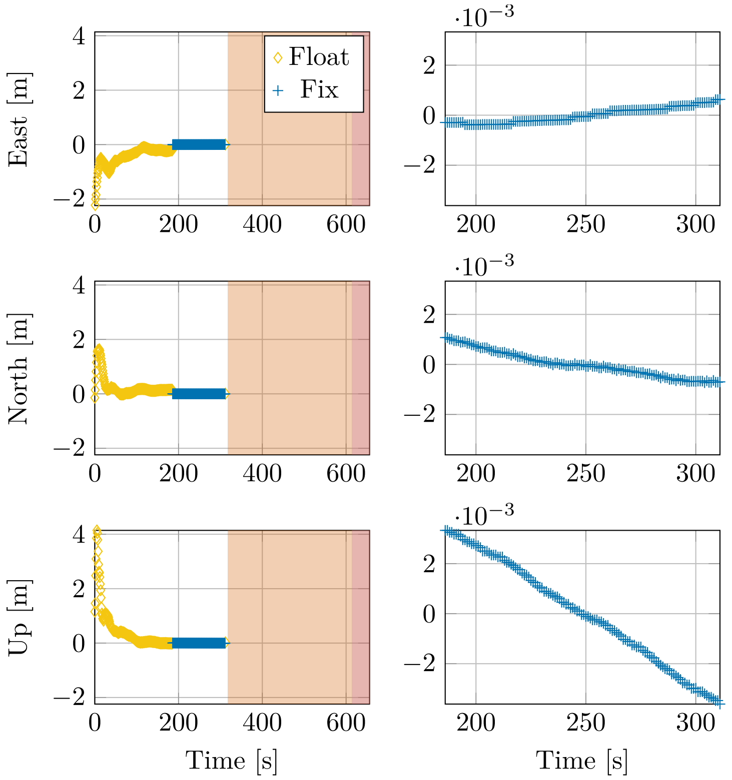

(b) Positioning solution of antenna 1 under jamming conditions using single antenna processing. Origin is the center of mass of all fix positions. Yellow points represent float solutions, blue points indicate fix solutions. Plots on the right-hand side are zoomed-in views of fix solutions from the respective axes on the left-hand side.

Figure 10: Measurement C: Distributed Subarray configuration Single-Antenna Processing

b) Measurement C: Distributed Subarrays Multi-Antenna Processing

Figure 11 illustrates the benefit of using multi-antenna processing over single antenna in a GNSS-denied environment. As one can see, there is a fall-down in the C/N_0 metric for all satellites once the jammer is turned on. However, this does not result in a complete loss of the satellites. We can observe the following:

- The signals from the satellite still reside at around 45 dBHz

- The IQRs of Figure 11 are much larger in comparison, suggesting a greater deviation between the signal strength across antennas.

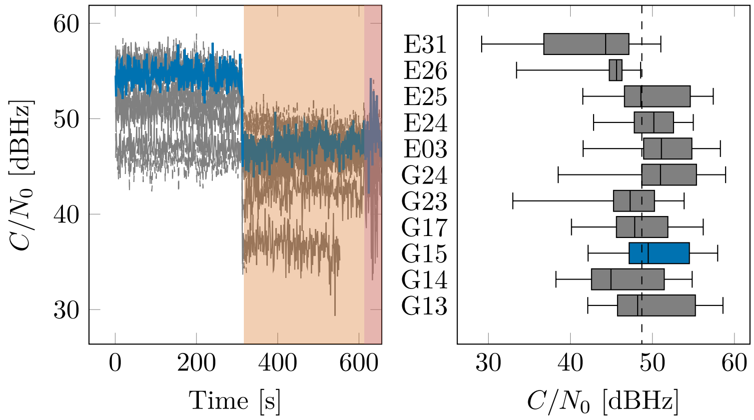

(a) Carrier-to-noise density ratios of the multi-antenna processing under subarray configuration with phase compensation in a GNSS-denied environment. On the left, the carrier-to-noise density ratios are plotted over time for reference Antenna 1. The orange tinted time interval indicates active static jamming. Magenta tinted time interval indicates active dynamic jamming. On the right, all carrier-to-noise density ratios from $N_{\text{ant}} = 4$ are collected. The dashed line represents the median C/N_0.

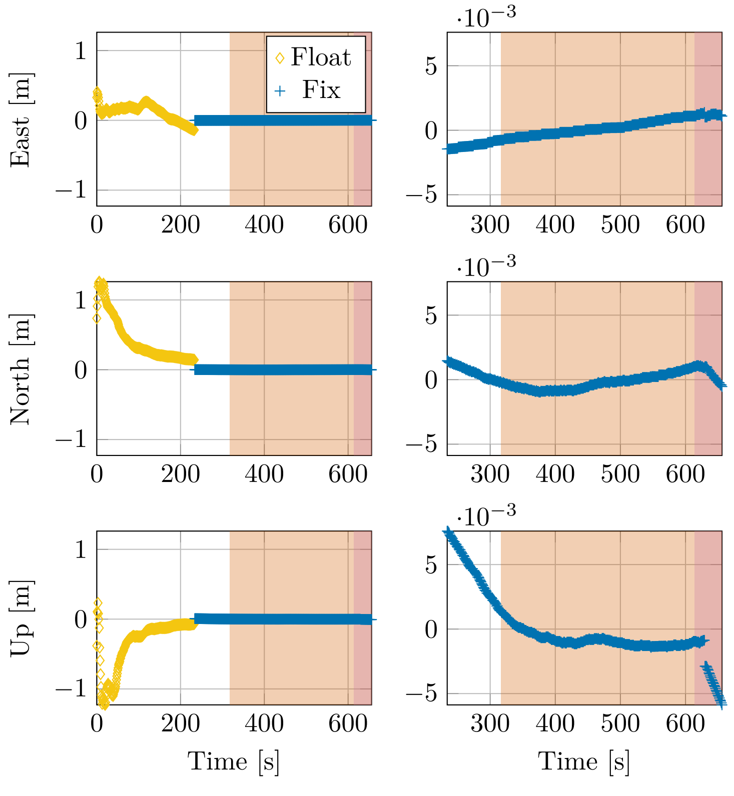

(b) Positioning solution of reference antenna 1 under jamming conditions using mutli-antenna spatial signal processing with phase compensation. Orange tinted area indicates active static jamming. Magenta tinted ara indicates active dynamic jamming. Origin is the center of mass of all fix positions. Yellow points represent float solutions, blue points indicate fix solutions. Plots on the right-hand side are zoomed-in views of fix solutions from the respective axes on the left-hand side.

Figure 11: Measurement C: Distributed Subarray configuration Multi-Antenna Processing

Further, Figure 11b illustrates that thanks to spatial signal processing a positioning solution is achieved. This is in sharp contrast to Figure 10b, where the fix solution is only achieved up until jamming is activated. Figure 11b in this sense presents a striking result, that subarray configured antenna arrays can achieve and hold an RTK fix under jamming. We can observe only fix positions on the right-hand side of the graph, notice the fix solution precision being in the ±5 mm range. Also notice that the fix positions worsen once the jammer antenna is moved around, as indicated by the magenta tinted area in the plot.

c) *Phase Compensation*

Figure 12b illustrates the effect that jamming has on the carrier phase residuals. The pivot satellite for the differences between the satellites in selected to be G15, the same PRN previously highlighted. We can see after the activation of the jammer, the carrier phase residuals start drifting away from zero. At the very end of the measurement, during the dynamic jamming scenario, a second step up in the carrier phase residual divergence is observed, and carrier phase residuals deviate further. Figure 12a contrasts Figure 12b, as it doesn't employ a phase compensation algorithm, like the one presented by Bamberg et al. (2022). Compared to Figure 12b, the carrier phase residuals deviate sharply at the time instance of jammer activation.

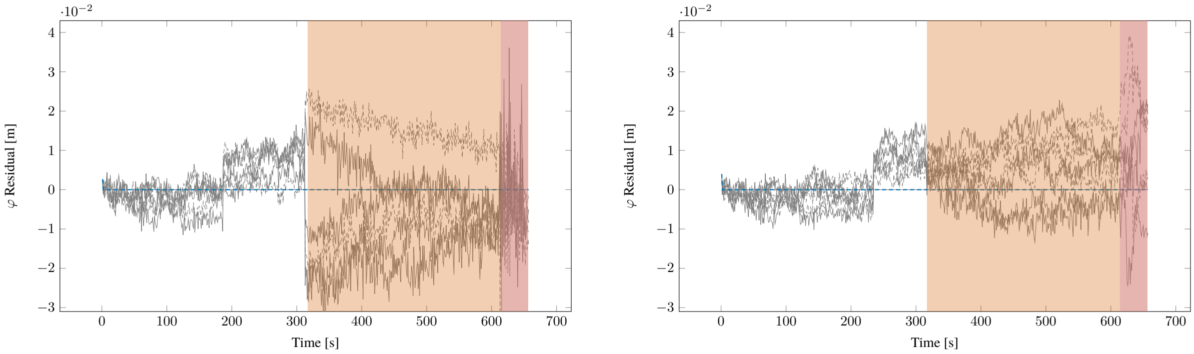

(a) *Without* a phase compensation algorithm

(b) *With* a phase compensation algorithm

Figure 12: Measurement C: Carrier-Phase Residuals. Orange tinted area indicates active static jamming. Magenta tinted area indicates active dynamic jamming.

d) *Statistical Analysis*

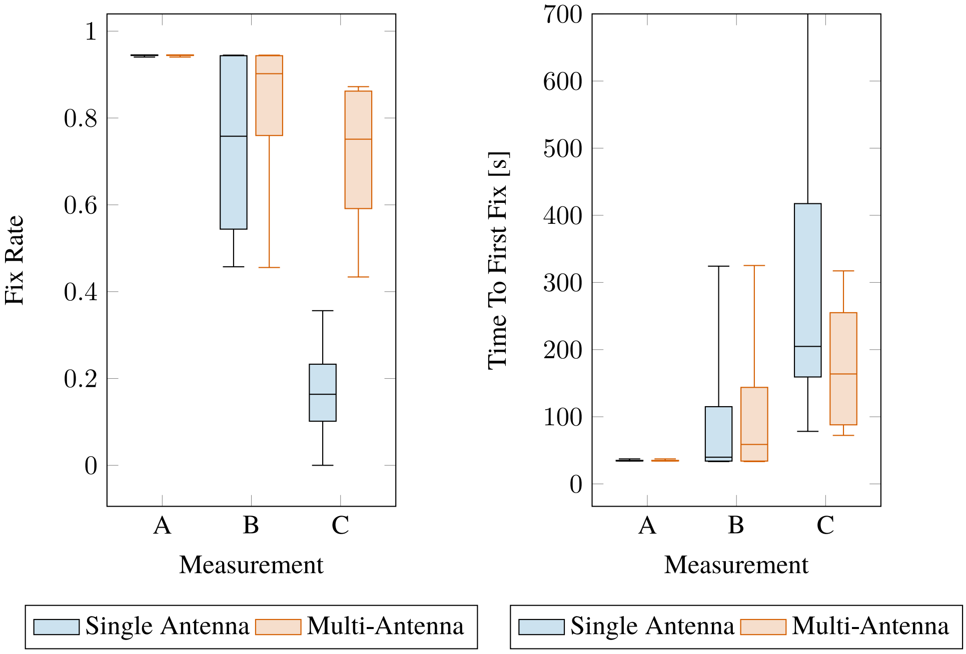

(a)

(b)

Figure 13: Fix rate (Figure 13a) and TTFF (Figure 13b) comparison between single antenna processing and multi-antenna spatial signal processing. Higher fix rates are better. Lower values of TTFF are better. Statistics were gathered from each measurement from $N_{\text{ant}} = 4$ antennas.

Yet another analysis that one can carry out on the measurement data is the evaluation of the *fix rate*. Fix rate is defined as the ratio between the number of epochs where an RTK fix has been achieved to the total number of epochs. Therefore, it is a dimensionless measure that can either be expressed $\in [0, 1]$ or as a percentage. Although not directly correlated, a high fix rate indicates a longer period of time for which receiver has been in an RTK fix state. However, the fix rate metric does not indicate, or punish for, fix losses that may occur after an initial fix and get rectified quickly. Nevertheless, it is a good measure for assessing general quality of the positioning solution from an RTK standpoint of view. As seen in Figure 13a, the fix rates vary between the various measurements conducted during the writing of this thesis. The x-Axis of the Figure indicates the measurements as they are assigned letters in Table 1. We can make the following conclusions from Figure 13a:

- Measurement A, conducted in a URA configuration, achieves a striking performance for both processing techniques, capping out at 95% fix rate.
- Measurement B is conducted in distributed subarray configuration. Here we can observe median fix rates of just under 80% for single antenna processing, and around 90% for the multi-antenna processing. The spread, indicated by the IQR body of the box is also much smaller for the multi-antenna processing, due to three out of four antennas achieving a fix rate higher than the median of single antenna processing.
- Measurement C, conducted under jamming conditions illustrates the benefit of using spatial signal processing. Due to the short time period of holding a fix position before getting jammed, the single antenna processing fix rate hover around 20%. Mutli-antenna spatial signal processing, being resilient to jamming, outperforms this figure vastly, by reaching the median value of 80%. This spread is expected to rise only further for longer periods of observations under jamming conditions.
- Summarizing the four measurements, we conclude that on average mulit-antenna processing outperformed single antenna processing fix rates, Single antenna processing exhibits a higher spread, covering the high fix rates achieved by multi-antenna processing $50\% - 90\%$, but also reaching as low down as 0% fix rates, stemming from jamming scenario. This shows multi-antenna spatially signal processed RTK solutions provide reliability even under jamming conditions and exotic antenna array setups, like the distributed subarray configuration.

TTFF (Time To First Fix) is another important metric gauging the ability of the receiver to achieve a fix position. Observing the values in Figure 13b we can reason the following conclusions:

- Measurement A, conducted under the URA configuration, outshines the subarray configured Measurements B and C. Here the TTFF is as low as 50 s for all antennas.
- Measurements B, C, however, do not fall far behind this high bar set by Measurement A, as in the best case these achieve similarly short TTFF of around 50 s.
- Measurement C, conducted under jamming conditions, shows an obvious advantage of the multi-antenna processing. The TTFF values for single antenna measurement are not clear about the quality of the overall solution here, as the fix was achieved before jamming commenced as shown in Figure 10b. The upper whisker is therefore off the chart here, for the case where the single antenna processing from Antenna 4 has not been able to achieve a fix before jamming was activated.

Lastly, if we consider solely the minimum values of all measurements in Figure 13b, we get times that are all under 150 s, which is a relatively good value.

V. CONCLUSION

This paper has introduced and demonstrated the functioning of high precision carrier-phase based RTK positioning in conjunction with interference resilient distributed antenna subarrays. A series of static measurements were conducted, testing the antennas in the traditional compact URA configuration (Measurement A), novel distributed subarray configuration (Measurement B), and the same subarray configuration under jamming conditions (Measurement C). Firstly, it has been demonstrated that distributed antenna subarrays are capable of achieving an RTK fix. The precision of the achieved fix is not worsened in comparison to a compact URA. Utilized two-step multi-antenna spatial signal processing algorithm also does not reduce the precision in comparison to the single antenna fix solutions. Generally speaking, the positioning solution fluctuates in the subcentimeter realm, around ±5 mm. In the event of jamming, the RTK fix is held stable throughout the jamming period, given the presented multi-antenna spatial signal processing approach is used. The precision of the positioning solution in this case is found to not worsen. Utilizing state-of-the-art phase compensation algorithms for the spatial signal processing algorithm has shown to improve the stability of carrier phase residuals drastically under jamming conditions, thus improving the ambiguity resolution capabilities of the whole system. The trade-off comes in at the expense of additional computational load and hardware required by multi-antenna system and the associated signal processing. Moreover, there is a marginal penalty observed throughout subarray measurements in comparison to the URA measurement concerning the fix rate and the time-to-first-fix metrics. At best the distributed subarrays system has achieved around 90% fix rate, and has converged in less than a minute. During jamming the median time to converge for a subarray system has been observed to be around 150 s with a median fix rate of around 80%. In contrast, the URA configuration has consistently achieved median values of 90% fix rate, and less than a minute convergence time. Nevertheless, we find the trade-offs to be justified considering the potential benefits of using distributed subarrays systems: bringing high precision positioning and resilience against GNSS interference closer to realistic autonomous application scenarios.

ACKNOWLEDGEMENTS

Parts of the research leading to the results reported in this paper have been funded within the project ROSANNA by the German Aerospace Center (DLR) on behalf of the German Federal Ministry for Economic Affairs and Energy under grant no. 50 NA 1901. and the project Galileo Protect by the DLR on behalf of the German Federal Ministry of Transport and Digital Infrastructure under grant no. 50 NP 2003. This support is greatly acknowledged.

REFERENCES

Bamberg, T., Konovaltsev, A., & Meurer, M. (2022). GNSS Antenna Arrays and RTK: The Effect of Carrier Phase Distortions Induced by Spatial Filtering on RTK Positioning. *Proceedings of the 2022 International Technical Meeting of The Institute of Navigation*, 799–811. https://doi.org/10.33012/2022.18161

Bamberg, T., Konovaltsev, A., & Meurer, M. (2023). Enabling RTK Positioning Under Jamming: Mitigation of Carrier-Phase Distortions Induced by Blind Spatial Filtering. *NAVIGATION: Journal of the Institute of Navigation*, *70*(1). https://doi.org/10.33012/navi.556

Bamberg, T., & Meurer, M. (2020). Carrier Phase Distortions with anti-jamming Techniques using GNSS Array Receivers. *WSA 2020; 24th International ITG Workshop on Smart Antennas*, 1–6.

Brachvogel, M., Niestroj, M., & Meurer, M. (2023). Full Wideband Calibration for an Array of Spatially Distributed Subarrays. *2023 IEEE/ION Position, Location and Navigation Symposium (PLANS)*, 1040–1048. https://doi.org/10.1109/PLANS53410.2023.10140050

Brachvogel, M., Niestroj, M., Schoenbrod, S., Meurer, M., Hasnain, S. N., Stephan, R., & Hein, M. A. (2021). Interference and Jammer Suppression of High Bandwidth Signals using an Array of Spatially Distributed Subarrays. *Proceedings of the 34th International Technical Meeting of the Satellite Division of The Institute of Navigation (ION GNSS+ 2021)*, 3812–3823. https://doi.org/10.33012/2021.18013

Brachvogel, M., Niestroj, M., Zorn, S., Meurer, M., Hasnain, S. N., Stephan, R., & Hein, M. A. (2020). A new array concept using spatially distributed subarrays for unambiguous GNSS interference mitigation in automotive applications. *NAVIGATION*, *67*(1), 23–41. https://doi.org/10.1002/navi.353

Clements, Z., Yoder, J. E., & Humphreys, T. E. (2022). Carrier-phase and IMU based GNSS Spoofing Detection for Ground Vehicles, 83–95. https://doi.org/10.33012/2022.18252

Cuntz, M., Konovaltsev, A., Hornbostel, A., Neves, E. S., & Dreher, A. (2007). GALANT - Galileo Antenna and Receiver Demonstrator for Safety-Critical Applications. *2007 European Conference on Wireless Technologies*, 59–61. https://doi.org/10.1109/ECWT.2007.4403945

Daneshmand, S., Marathe, T., & Lachapelle, G. (2016). Millimetre Level Accuracy GNSS Positioning with the Blind Adaptive Beamforming Method in Interference Environments. *Sensors*, *16*(11), 1824. https://doi.org/10.3390/s16111824

EUSPA. (2022). *EUSPA EO and GNSS Market Report*. EUSPA. Retrieved March 9, 2023, from https://www.euspa.europa.eu/sites/default/files/uploads/euspa_market_report_2022.pdf

Gao, G. X., Heng, L., Hornbostel, A., Denks, H., Meurer, M., Walter, T., & Enge, P. (2013). DME/TACAN interference mitigation for GNSS: Algorithms and flight test results. *GPS Solutions*, *17*(4), 561–573. https://doi.org/10.1007/s10291-012-0301-9

Gao, G. X., Sgammini, M., Lu, M., & Kubo, N. (2016). Protecting GNSS Receivers From Jamming and Interference. *Proceedings of the IEEE*, *104*(6), 1327–1338. https://doi.org/10.1109/JPROC.2016.2525938

Groves, P. D. (2008). *Principles of GNSS, inertial, and multisensor integrated navigation systems* (1st ed.). Artech House.

Kappen, G. C., Zhang, S., Liu, S., Biermann, M., Gemmeke, T., & Borgmann, D. (2022). secRTK -A Jamming Resistant RTK-Receiver: Prototype Architecture and Results of First Measurement Campaigns. *2022 10th Workshop on Satellite Navigation Technology (NAVITEC)*, 1–8. https://doi.org/10.1109/NAVITEC53682.2022.9847552

Kay, S. M. (1993). *Fundamentals of Statistical Signal Processing: Estimation theory*. Prentice Hall PTR.

Medina, D., Vilà-Valls, J., Hesselbarth, A., Ziebold, R., & García, J. (2020). On the Recursive Joint Position and Attitude Determination in Multi-Antenna GNSS Platforms. *Remote Sensing*, *12*(12), 1955. https://doi.org/10.3390/rs12121955

Morales-Ferre, R., Richter, P., Falletti, E., de la Fuente, A., & Lohan, E. S. (2020). A Survey on Coping With Intentional Interference in Satellite Navigation for Manned and Unmanned Aircraft. *IEEE Communications Surveys & Tutorials*, *22*(1), 249–291. https://doi.org/10.1109/COMST.2019.2949178

Osechas, O., Fohlmeister, F., Dautermann, T., & Felux, M. (2022). Impact of GNSS-Band Radio Interference on Operational Avionics. *NAVIGATION: Journal of the Institute of Navigation*, *69*(2). https://doi.org/10.33012/navi.516

Pullen, S., & Gao, G. X. (2012). GNSS Jamming in the Name of privacy potential Threat to GPS aviation [magazine]. *InsideGNSS*, 34–43. https://www.insidegnss.com/auto/marapr12-Pullen.pdf

Reid, T. G., Houts, S. E., Cammarata, R., Mills, G., Agarwal, S., Vora, A., & Pandey, G. (2019). Localization Requirements for Autonomous Vehicles. *SAE International Journal of Connected and Automated Vehicles*, *2*(3), 12-02-03–0012. https://doi.org/10.4271/12-02-03-0012

Sgammini, M., Antreich, F., Kurz, L., Meurer, M., & Noll, T. G. (2012). Blind Adaptive Beamformer Based on Orthogonal Projections for GNSS. Retrieved October 20, 2022, from https://elib.dlr.de/81073/

Takasu, T. (2013, April 29). RTKLIB ver. 2.4.2 Manual. *rtklib.com*. Retrieved March 6, 2023, from https://www.rtklib.com/prog/manual_2.4.2.pdf

Taşdemir, E., Ascheid, G., & Noll, T. G. (2018). *Blind interference mitigation in multi-antenna GNSS receivers* (Publication No. RWTH-2018-226786). Retrieved October 26, 2022, from https://publications.rwth-aachen.de/record/730322

Van Trees. (2002). *Optimum Array Processing: Part IV of Detection, Estimation, and Modulation Theory* (1st ed.). John Wiley & Sons, Inc. https://doi.org/10.1002/0471221104

Yoder, J. E., & Humphreys, T. E. (2023). Low-Cost Inertial Aiding for Deep-Urban Tightly Coupled Multi-Antenna Precise GNSS. *NAVIGATION: Journal of the Institute of Navigation*, *70*(1), navi.561. https://doi.org/10.33012/navi.561

Zorn, S., Niestroj, M., Caizzone, S., Brachvogel, M., & Meurer, M. (2017). Self-contained Antenna Crosstalk and Phase Offset Calibration by Jointly Solving the Attitude Estimation and Calibration Problem, 3481–3493. https://doi.org/10.33012/2017.15382